

# Lattice Boltzmann study on thermoacoustic onset in a Rijke tube

Yong Wang<sup>1,2,a</sup>, Dong-Ke Sun<sup>3,b</sup>, Ya-Ling He<sup>1,c</sup>, and Wen-Quan Tao<sup>1,d</sup>

<sup>1</sup> Key Laboratory of Thermo-Fluid Science and Engineering of MOE, School of Energy and Power Engineering, Xi'an Jiaotong University, Xi'an, Shaanxi 710049, China

<sup>2</sup> Department of Mechanical and Aerospace Engineering, University of California, Irvine, CA 92697, USA

<sup>3</sup> Jiangsu Key Laboratory for Design and Manufacture of Micro-Nano Biomedical Instruments, School of Mechanical Engineering, Southeast University, Nanjing 211189, China

Received: 9 July 2014 / Revised: 14 November 2014

Published online: 23 January 2015 – © Società Italiana di Fisica / Springer-Verlag 2015

**Abstract.** Nonlinear thermoacoustic self-excited onset was numerically studied in this work. A lattice Boltzmann model for viscous compressible flow and the implicit-explicit finite difference method were used to develop a solver. Nonlinear onset in an open-open Rijke tube with a constant-temperature stack was simulated with the solver. Based on the numerical results, overall onset process and self-excited standing wave in the Rijke tube are observed. The length of the Rijke tube along the  $x$ -direction covers a  $1/4$  wavelength of the standing wave and the main component of this standing wave is 171.2 Hz. These results agree well with the theoretical prediction. Instantaneous velocity and temperature fields at several phases under the limit cycle are presented and discussed. The maximal Mach number is about 0.035, indicating that the flow in the Rijke tube is a low Mach number compressible flow. This solver can also be applied for simulations of some other complex flows, such as the flow in porous media stack in thermoacoustic engine.

## 1 Introduction

Thermoacoustics can be simplistically defined as the physics of the interaction of thermal and acoustic fields [1], and has been attracting more and more attention as a major technology in the development of high efficient energy conversion/generation systems. However, the nonlinear acoustic effect, the space and time multi-scale effect, the low Mach number compressible flow and the flow within porous media in the thermoacoustic engines make it very complicated in theory. Therein, self-excited thermoacoustic onset is one of the most typical nonlinear phenomena. Thermoacoustic engine can only achieve the conversion of thermal energy to mechanical energy after the process of thermoacoustic onset. As a result, thermoacoustic onset has gotten more and more attention in the academic community [2–8]. An example of the thermoacoustic nonlinear onset is the Rijke tube [6], which is a straight tube with heated stacks placed inside. Understanding of gas oscillating patterns in the Rijke tube is of both fundamental and practical importance. Both the nonlinear acoustic effect and the low Mach number compressible flow can be observed in the Rijke tube. Theoretical and experimental investigations on the Rijke tube can be found in refs. [9–12] and references therein. To the best of our knowledge, numerical studies on it can be classified into two different categories. For the first one, only the region inside the Rijke tube is considered as the computational domain. Hantschk and Vortmeyer firstly simulated the Rijke tube with this idea [2,3]. The temperature of the stacks in the Rijke tube was considered as a constant in their simulations. Then, Chatterjee *et al.* investigated the occurrence of combustion instabilities in a Rijke tube type of combustor with the same idea [12]. For the second one, both the region inside the Rijke tube and some additional region outside are considered as the computational domain. Physical boundaries of the open sides of the Rijke tube are then treated as internal region in the computational domain. Entezam *et al.*'s study belongs to this category [4]. In comparison with these two categories, the first one needs more attention on the treatment of the boundary conditions, whereas a much more computational resource is needed for the second one, due to the extension of the computational domain. At the same time, all simulations on the Rijke tube mentioned

<sup>a</sup> e-mail: ywangcam@gmail.com

<sup>b</sup> e-mail: dongke.sun@gmail.com

<sup>c</sup> e-mail: yalinghe@mail.xjtu.edu.cn

<sup>d</sup> e-mail: wqtao@mail.xjtu.edu.cn

above were performed using commercial softwares with conventional computational fluid dynamics (such as the finite volume method and finite difference method). Specifically, Flow-3D was used in ref. [4], and Fluent was used in the other references.

The lattice Boltzmann method (LBM) is an alternative and promising numerical method for studying thermoacoustic problems. The LBM was originated in the wake of its ancestor, the lattice gas automata method, and improved greatly in response to its initial drawbacks [13]. The LBM was first introduced by McNamara and Zanetti [14], and is different from the conventional numerical methods solving the macroscopic governing equations, *e.g.* Navier-Stokes-Fourier (NSF) equations for the conserved fields. Based on the kinetic theory, the LBM simulates fluid flows by tracking the evolution of particles taking on a few discrete velocities in discrete space at discrete time steps. It can easily model fluid flows with complicated boundary conditions. This means the LBM provides a method to obtain flow streams and heat transfer patterns for complicated systems (in the thermoacoustic engine, such as flow in porous media stack and low Mach number compressible flow) from the microscopic and kinetic level [15–20]. Other merits of the LBM are the localization and easy implementation of its computational scheme. Considering its advantages mentioned above, we adopted the LBM to study phenomena systematically in the thermoacoustic engine. Our previous efforts can be found in refs. [21, 22], in which we studied the gas oscillation in a resonator by the standard LBM and the finite difference LBM (FDLBM), respectively.

This work presents a numerical study on the nonlinear self-excited thermoacoustic onset in a Rijke tube with the LBM model for viscous compressible flow [23] and the implicit-explicit (IMEX) FDLBM [24] presented in our previous papers. The numerical solver used here is developed with the FORTRAN language. This paper is organized as follows. In sect. 2, details of the LBM model for viscous compressible flow and the IMEX FDLBM are introduced. In sect. 3, physical model of the Rijke tube and simulation details are presented. Numerical results and corresponding discussions are given in sect. 4. A brief conclusion of the present study is given in sect. 5.

## 2 Formulation of the LBM

In our previous work, a LBM model based on a polynomial kernel function in the phase space was developed for viscous compressible flows with flexible specific-heat ratio and Prandtl number [23]. Density distribution function (DF)  $f$  and total energy DF  $h$  are used in this model. Corresponding equilibrium DFs are obtained from the discretization of the polynomial kernel function with Lagrangian interpolation and be coupled via the equation of state for gas. The evolution equations of these two DFs are the discrete Boltzmann equations with the BGK approximation

$$\frac{\partial f_i}{\partial t} + \mathbf{e}_i \cdot \nabla f_i = -\frac{1}{\tau_f} (f_i - f_i^{\text{eq}}), \quad (1a)$$

$$\frac{\partial h_i}{\partial t} + \mathbf{e}_i \cdot \nabla h_i = -\frac{1}{\tau_h} (h_i - h_i^{\text{eq}}) + \frac{\mathbf{e}_i \cdot \mathbf{u}}{\tau_{hf}} (f_i - f_i^{\text{eq}}), \quad (1b)$$

where  $f_i$  and  $h_i$  are the discrete density DF and the discrete total energy DF, respectively;  $f_i^{\text{eq}}$  and  $h_i^{\text{eq}}$  are their corresponding equilibrium DFs;  $\mathbf{e}_i$  is the discrete velocities;  $i = 0, \dots, \mathcal{N} - 1$ ,  $\mathcal{N}$  is the total number of discrete velocities;  $t$  and  $\mathbf{u}$  are the macroscopic time and velocity, respectively;  $\tau_f$  and  $\tau_h$  are the relaxation times for momentum and energy transport, respectively, and  $\tau_{hf} = \tau_h \tau_f / (\tau_f - \tau_h)$ .

A two-dimensional version of this model with a D2Q13 lattice (see fig. 1,  $\mathcal{N} = 13$ ) is given as below. The discrete velocities of the D2Q13 lattice are

$$\frac{\mathbf{e}_i}{\sqrt{RT_c}} = \begin{cases} (0, 0), & i = 0 \\ \text{cyc} : (\pm 1, 0), & i = 1, 2, 3, 4 \\ \text{cyc} : \sqrt{2}(\pm 1, \pm 1), & i = 5, 6, 7, 8 \\ \text{cyc} : 2(\pm 1, 0), & i = 9, 10, 11, 12 \end{cases}, \quad (2)$$

where cyc indicates the cyclic permutation;  $T_c$  is the characteristic temperature. In order to avoid extrapolation,  $|\mathbf{u}| + c < \sqrt{2RT_c}$  should be ensured, where  $c$  is the effective peculiar velocity and  $\sqrt{2RT_c}$  is the shortest distance from the origin to the edges of the lattice.  $R$  is the gas constant and  $T$  is the temperature of gas.

The discrete equilibrium density DF  $f_i^{\text{eq}}$  of this model is defined as a function of the macroscopic density, velocity and temperature as

$$f_0^{\text{eq}}(u, v) = \frac{\rho}{4} \left[ 4 - 10\bar{T} + 10\bar{T}^2 + (10\bar{T} - 5)(\bar{u}^2 + \bar{v}^2) + \bar{u}^4 + 4\bar{u}^2\bar{v}^2 + \bar{v}^4 \right], \quad (3a)$$

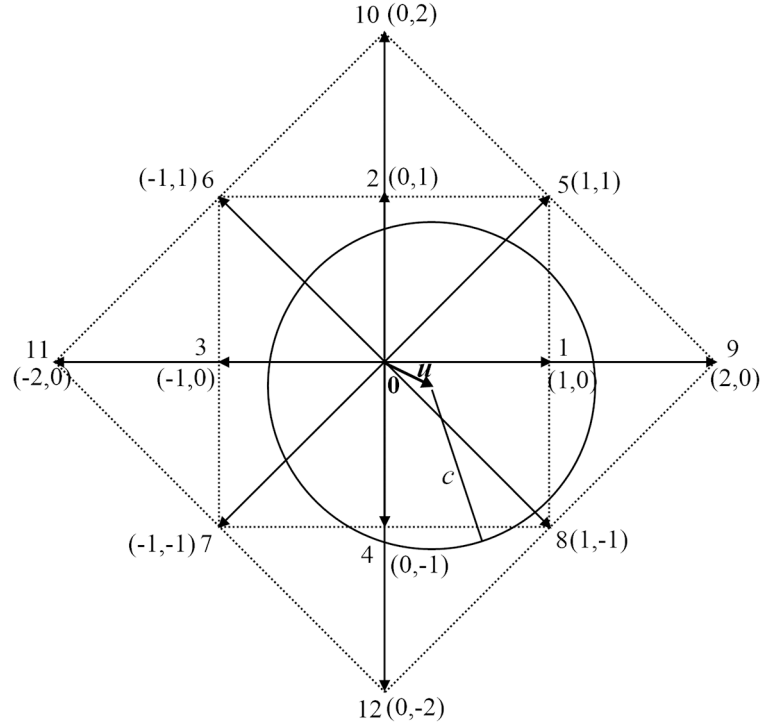


**Fig. 1.** Configuration of the D2Q13 lattice.

$$f_1^{eq}(u, v) = \frac{\rho}{6} [(4 - 6\bar{T})(\bar{T} + \bar{u} + \bar{u}^2) - 3\bar{T}(\bar{u}^2 + \bar{v}^2) - (\bar{u} + \bar{u}^2)(\bar{u}^2 + 3\bar{v}^2)], \quad (3b)$$

$$f_5^{eq}(u, v) = \frac{\rho}{4} [(\bar{T} + \bar{u} + \bar{u}^2)(\bar{T} + \bar{v} + \bar{v}^2)], \quad (3c)$$

$$f_9^{eq}(u, v) = \frac{\rho}{24} [-\bar{T} + 3\bar{T}^2 - (2 - 6\bar{T})\bar{u} - (1 - 6\bar{T})\bar{u}^2 + 2\bar{u}^3 + \bar{u}^4], \quad (3d)$$

and

$$f_2^{eq}(u, v) = f_1^{eq}(v, u), \quad f_3^{eq}(u, v) = f_1^{eq}(-u, v), \quad f_4^{eq}(u, v) = f_1^{eq}(-v, u), \quad (3e)$$

$$f_6^{eq}(u, v) = f_5^{eq}(-u, v), \quad f_7^{eq}(u, v) = f_5^{eq}(-u, -v), \quad f_8^{eq}(u, v) = f_5^{eq}(u, -v), \quad (3f)$$

$$f_{10}^{eq}(u, v) = f_9^{eq}(v, u), \quad f_{11}^{eq}(u, v) = f_9^{eq}(-u, v), \quad f_{12}^{eq}(u, v) = f_9^{eq}(-v, u). \quad (3g)$$

Here,  $f_i^{eq}(u, v)$  is the abbreviation of  $f_i^{eq}(\rho, u, v, T)$ ;  $\bar{T}$ ,  $\bar{u}$  and  $\bar{v}$  are defined as  $\bar{T} = T/T_c$  and  $(\bar{u}, \bar{v}) = (u, v)/\sqrt{RT_c}$ .  $f_2^{eq}(u, v) = f_1^{eq}(v, u)$  means  $f_2^{eq}(u, v)$  is calculated with the same form of  $f_i^{eq}(u, v)$ , and the locations of the parameters in  $f_i^{eq}(u, v)$  are permuted. Similarly, the discrete equilibrium total energy DF  $h_i^{eq}$  is

$$h_0^{eq} = \frac{\rho RT_c}{24} [A_0 + A_1(\bar{u}^2 + \bar{v}^2) + A_2(\bar{u}^4 + \bar{v}^4) + A_3\bar{u}^2\bar{v}^2 + 3(\bar{u}^6 + \bar{v}^6) + 15(\bar{u}^4\bar{v}^2 + \bar{u}^2\bar{v}^4)], \quad (4a)$$

$$h_1^{eq} = \frac{\rho RT_c}{12} [B_0 + B_1\bar{u} + B_2\bar{u}^2 + B_3\bar{v}^2 + B_4\bar{u}^3 + B_5\bar{u}\bar{v}^2 + B_6\bar{u}^4 + B_7\bar{u}^2\bar{v}^2 - 3T\bar{v}^4 - (\bar{u} + \bar{u}^2)(\bar{u}^4 + 3\bar{v}^4 + 4\bar{u}^2\bar{v}^2)], \quad (4b)$$

$$h_5^{eq} = \frac{\rho RT_c}{24} [C_0 + C_1(\bar{u} + \bar{v}) + C_2(\bar{u}^2 + \bar{v}^2) + C_3\bar{u}\bar{v} + C_4(\bar{u}\bar{v}^2 + \bar{u}^2\bar{v}) + C_5\bar{u}^2\bar{v}^2 + 3T \times (\bar{u}^3 + \bar{v}^3 + \bar{u}^4 + \bar{v}^4) + 3\bar{u}\bar{v}(\bar{u}^2 + \bar{v}^2 + \bar{u}^3 + \bar{v}^3) + 3\bar{u}^2\bar{v}^2(\bar{u} + \bar{v} + \bar{u}^2 + \bar{v}^2)], \quad (4c)$$

$$h_9^{eq} = \frac{\rho RT_c}{48} [-G_0 - G_1\bar{u} - G_2\bar{u}^2 - G_3\bar{v}^2 - G_4\bar{u}^3 - G_5\bar{u}\bar{v}^2 - G_6\bar{u}^4 - G_7\bar{u}^2\bar{v}^2 + (2\bar{u}^3 + \bar{u}^4)(\bar{u}^2 + \bar{v}^2)], \quad (4d)$$

where coefficients  $A_0 \dots A_3, B_0 \dots B_6, C_0 \dots C_4, G_0 \dots G_7$  are given in table 1. Besides eq. (4), other parts of the discrete equilibrium total energy DF can be obtained with the same relations shown in eqs. (3e)–(3g). It can be found that eqs. (3) and (4) are polynomials up to the fourth and sixth order of the macroscopic velocity  $\mathbf{u}$ , respectively.

**Table 1.** Coefficients in the discrete equilibrium total energy DF  $h_i^{\text{eq}}$  given by eq. (4).

$i$	Coefficients
0	$A_0 = (24 + 12K - 120\bar{T} - 30K\bar{T} + 160\bar{T}^2 + 30K\bar{T}^2)\bar{T}$ , $A_1 = 12 - 120\bar{T} - 15K\bar{T} + 270\bar{T}^2 + 30K\bar{T}^2$ $A_2 = -15 + 60\bar{T} + 3K\bar{T}$ , $A_3 = -30 + 180\bar{T} + 12K\bar{T}$
1	$B_0 = (B_{1,1} + 4\bar{T})\bar{T}$ , $B_1 = (16 + 4K - 36\bar{T} - 6K\bar{T})\bar{T}$ , $B_2 = (28 + 4K - 78\bar{T} - 9K\bar{T})\bar{T}$ , $B_3 = B_5\bar{T}$ , $B_4 = B_6 + 5\bar{T}$ , $B_5 = 4 - 30\bar{T} - 3K\bar{T}$ , $B_6 = 4 - 19\bar{T} - K\bar{T}$ , $B_7 = B_5 - 12\bar{T}$
5	$C_0 = (16 + 3K)\bar{T}^3$ , $C_1 = C_3\bar{T}$ , $C_2 = C_4\bar{T}$ , $C_3 = C_4 - 9\bar{T}$ , $C_4 = (27 + 3K)\bar{T}$ , $C_5 = C_4 + 9\bar{T}$
9	$G_0 = (G_1/2 + 2)\bar{T}$ , $G_1 = (8 + 2K - 36\bar{T} - 6K\bar{T})\bar{T}$ , $G_2 = (7 + K - 51\bar{T} - 6K\bar{T})\bar{T}$ , $G_3 = (1 - 3\bar{T})\bar{T}$ , $G_4 = 2G_6 + 10\bar{T}$ , $G_5 = 2 - 6\bar{T}$ , $G_6 = 1 - 16\bar{T} - K\bar{T}$ , $G_7 = G_5 - 1$

The macroscopic density  $\rho$ , velocity  $\mathbf{u}$ , temperature  $T$  can be calculated in terms of the DFs as follows:

$$\rho = \sum_i f_i, \quad (5a)$$

$$\mathbf{u} = \sum_i f_i \mathbf{e}_i / \rho, \quad (5b)$$

$$T = 2 \left( \sum_i h_i / \rho - |\mathbf{u}|^2 / 2 \right) / bR, \quad (5c)$$

where  $b$  is a constant related to the specific-heat ratio  $\gamma$  by  $\gamma = (b + 2)/b$ . With the Chapman-Enskog expansion, the NSF equations can also be derived from moments of eq. (1) in the limit of slow variations in space and time. The obtained macroscopic equations are given as follows:

$$\frac{\partial \rho}{\partial t} + \frac{\partial \rho u_\alpha}{\partial x_\alpha} = 0, \quad (6a)$$

$$\frac{\partial \rho u_\alpha}{\partial t} + \frac{\partial \rho u_\alpha u_\beta}{\partial x_\beta} + \frac{\partial p}{\partial x_\alpha} = \frac{\partial P'_{\alpha\beta}}{\partial x_\beta}, \quad (6b)$$

$$\frac{\partial \rho E}{\partial t} + \frac{\partial (\rho E + p) u_\alpha}{\partial x_\alpha} = \frac{\partial}{\partial x_\beta} \left( \lambda \frac{\partial T}{\partial x_\beta} + P'_{\alpha\beta} u_\alpha \right), \quad (6c)$$

and

$$p = \rho RT, \quad (6d)$$

$$P'_{\alpha\beta} = \mu \left( \frac{\partial u_\alpha}{\partial x_\beta} + \frac{\partial u_\beta}{\partial x_\alpha} - \frac{2}{D} \frac{\partial u_\chi}{\partial x_\chi} \delta_{\alpha\beta} \right) + \mu_B \frac{\partial u_\chi}{\partial x_\chi} \delta_{\alpha\beta}, \quad (6e)$$

where  $\mu$ ,  $\mu_B$  and  $\lambda$  are the dynamic viscosity, the bulk viscosity and the thermal conductivity, respectively, and defined as

$$\mu = \tau_f p, \quad \mu_B = (2/D - 2/b) \tau_f p, \quad \lambda = \tau_h c_p p. \quad (7)$$

Here,  $D$  is the spatial dimension;  $c_p = (b + 2)R/2$  is the specific heat at constant pressure and the Prandtl number is  $Pr = \mu c_p / \lambda = \tau_f / \tau_h$ .

To solve eq. (1) numerically, the IMEX FDLBM [24] is adopted. It has been demonstrated that, by using this method, problems (no matter stiff or not) can be integrated quickly with moderate Courant-Friedrich-Lewy (CFL) number, which is defined as  $C_{\text{CFL}} = \Delta t \cdot \max(e_{ix}, e_{iy}) / \min(\Delta x, \Delta y)$ . Here,  $\Delta t$  is the time spacing;  $\Delta x$  and  $\Delta y$  are the mesh spacing steps in the  $x$ - and  $y$ -direction, respectively. Details about the IMEX Runge-Kutta scheme and the difference schemes in the LBM can be found in ref. [24]. Moreover, one may notice that the compressible mode originally developed by Kataoka and Tsutahara [25] was used in ref. [24]. A D2Q16 lattice was used in that model and a variable related to the rest energy, which comes from the internal motion of molecules, was introduced to control the specific heat. Compared with the D2Q16 model, the model with double distribution functions used here is more stable in a large range of Mach number, as discussed in ref. [23].

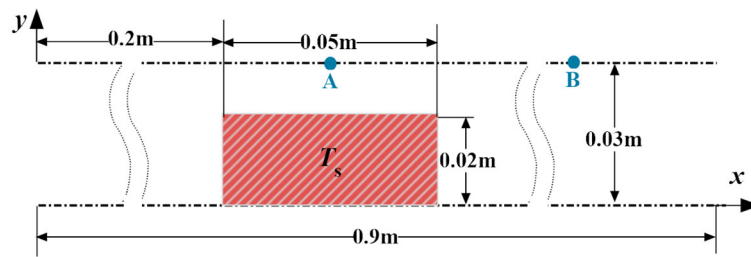


Fig. 2. Schematic description of the Rijke tube.

### 3 Physical model and simulation details

A numerical simulation was performed for the nonlinear self-excited onset in a Rijke tube via the LBM solver introduced in sect. 2. A Rijke tube with  $L = 0.9\text{m}$  in length and two openings is considered, as shown in fig. 2. A stack with cross-section  $0.05\text{m} \times 0.02\text{m}$  and constant temperature  $T_s = 1000\text{K}$  is placed at  $x = 0.225\text{m}$  ( $= L/4$ ). Considering a realistic condition in the experiment, the heated air in a vertical Rijke tube will float and fresh air in the outside environment will be inhaled continuously. A constant flow with velocity  $u_{\text{in}} = 0.1\text{m/s}$  in the  $x$ -direction is prescribed at the left inlet ( $x = 0\text{m}$ ) to mimic the inflow of fresh air. Symmetric boundaries are applied in the  $y$ -direction (upper and lower) to mimic various parallel stacks. Then, a standing wave with a wavelength of  $4L$  will be excited in this open-open Rijke tube due to the thermoacoustic effect.

In the simulation, only the region inside the Rijke tube is considered as the computational domain. We assume that the fluid is air under normal condition, and use  $\rho_0 = 1.165\text{kg/m}^3$ ,  $T_0 = 293\text{K}$ ,  $\mu = 1.86 \times 10^{-5}\text{kg/(m}\cdot\text{s)}$ ,  $R = 287\text{J/(kg}\cdot\text{K)}$  and  $P_0 = \rho_0 RT_0$ .  $b = 5$  is set to get  $\gamma = 1.4$ .  $Pr$  is set to be  $0.071$ , which is one tenth of the normal value  $0.71$  of the air, for the purpose of accelerating heat convection. A mesh with  $N_x \times N_y = 900 \times 17$  is adopted after mesh-independent test, where  $N_x$  and  $N_y$  are the lattice numbers along the  $x$ - and  $y$ -direction, respectively.

Boundaries are treated carefully in the solver. At the inlet ( $x = 0\text{m}$ ), the velocity and temperature of the air are given as  $u_{\text{in}}$  and  $T_0$ , respectively, and the pressure is extrapolated from that of the internal nodes. At the outlet ( $x = 0.9\text{m}$ ), both the velocity and temperature are extrapolated from the internal corresponding values, and the pressure is set to be constant  $P_0$ . Densities on both left and right boundaries are calculated with the equation of the state for gas. The nonequilibrium extrapolation method [26] is then applied to calculate unknown DFs on the two boundaries. In the  $y$ -direction, the symmetric boundary condition is adopted at both the upper and lower boundaries and the DFs on the boundary nodes can be obtained directly from the ones on the closest internal nodes.

The tube is initialized with static air. The pressure is uniform and set to  $P_0$ . The temperature in the left region ( $0 \leq x \leq 0.2\text{m}$ ) of the Rijke tube is  $T_0$ , and the other region  $(T_0 + T_s)/2$ . Moreover, variable properties of the air are considered. The viscosity and the thermal conductivity change linearly with the change of the temperature.

Based on the previous research [5], we believe that for simulation of the thermoacoustic onset, time step and numerical scheme for time marching are main factors effecting numerical stability and numerical resolution. However, much smaller time step and higher-order time scheme lead to considerable computational requirement even for modern computer. As a result, the second-order IMEX Runge-Kutta scheme [24,27] and the second-order upwind difference scheme [23] are adopted for the time and space discretizations, respectively. Some important parameters are  $T_c = 10T_0$ , and  $C_{\text{CFL}} = 0.734$  with  $\delta_t = 4 \times 10^{-7}\text{s}$ . Shared memory programming with OpenMP was used to develop our solver. As to the current Rijke tube, the computation time used is about 4 days with 8 Intel processors (2.33 GHz).

### 4 Results and discussions

Nonlinear onset process is presented firstly. Figure 3 gives the time histories of the pressure and velocity at point A ( $x = 0.225\text{m}$ ,  $y = 0.003\text{m}$ ) and provides an idea of the overall onset process. As the initial state of the Rijke tube is not the equilibrium one, the amplitudes of the pressure and velocity will decrease in an initial period lasting about  $0.5\text{s}$ . Then a rapid increase in the oscillation amplitudes can be found and nonlinear onset occurs due to the thermoacoustic effect. After  $t = 3.5\text{s}$ , the amplitudes of the pressure and velocity no longer change and the Rijke tube reaches its corresponding limit cycle state.

Figure 4 presents the time histories of pressure and temperature at point B ( $x = 0.575\text{m}$ ,  $y = 0.003\text{m}$ ). In comparison with figs. 4(a) and 3(a), the pressure at point B has similar developing process as that at point A. However, the amplitude under the limit cycle condition at point A (upper the stack) is larger than that at point B (right side of the stack). From fig. 4(b), it can also be found that temperature at point B varies very small in the initial period ( $0\text{--}0.5\text{s}$ ). After the initial period, heat convection is enhanced due to the thermoacoustic effect and the air at the right side of the stack was heated. Then, the corresponding temperature rises rapidly and oscillates small around  $960\text{K}$  under the limit cycle condition.

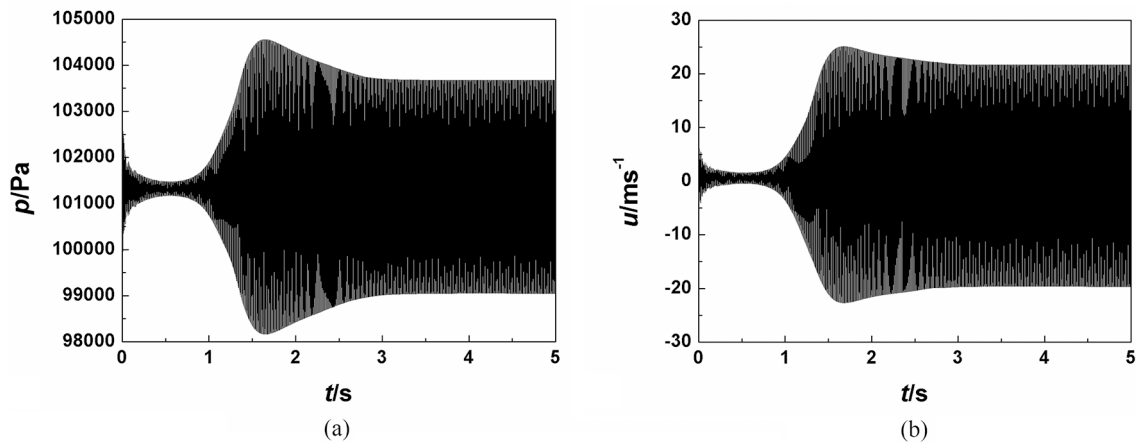


**Fig. 3.** Time histories of the (a) pressure and (b) velocity at point A ( $x = 0.225$  m,  $y = 0.003$  m).

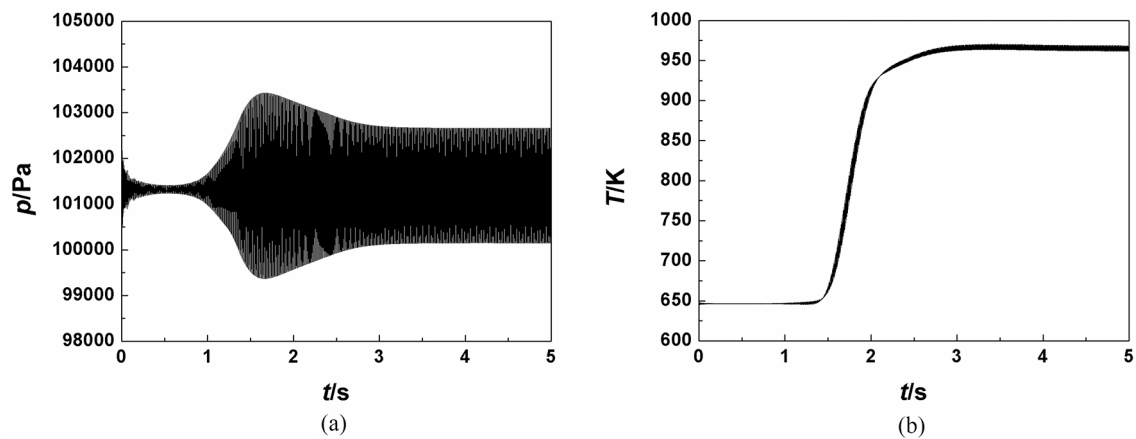


**Fig. 4.** Time histories of the (a) pressure and (b) temperature at point B ( $x = 0.575$  m,  $y = 0.003$  m).

Flow characteristics under the limit cycle condition are presented and discussed below. The wave forms of the pressure and velocity under the limit cycle condition at point A ( $x = 0.225$  m,  $y = 0.003$  m) are presented in fig. 5. It can be observed that the phase difference between the pressure and velocity is about  $1/4$  cycle (or  $\pi/2$ ), as to be expected for standing wave. Furthermore, fast Fourier transform (FFT) of the pressure signal at the same location is carried out. It can be observed from fig. 6 that the main component of the pressure signal is 171.2 Hz. Considering most air in the Rijke tube will be heated to 960 K, the sound speed in the Rijke tube is about 621.1 m/s. The fundamental frequency of the air system is then 172.5 Hz in theory. It can be seen that numerical results agree well with the theoretical prediction.

Figure 7 refers the instantaneous distributions of the pressure and velocity along the  $x$ -direction of the Rijke tube under the limit cycle condition at  $y = 0.003$  m. Eight phases (moments) in an oscillating cycle are presented. The state with averaged pressure and minimal velocity is considered as the phase 0. From fig. 7, it can be seen that the physical parameters of the air are fluctuant, and inverse flow can be found due to harmonic vibration of the air. Figure 7 also indicates the length of the Rijke tube along the  $x$ -direction covers a  $1/4$  wavelength of the standing wave. The wave loop of the oscillating pressure and wave node of the velocity are located at the left inlet of the Rijke tube, whereas the wave node of the pressure and wave loop of the velocity are located at the right. Moreover, one can see from fig. 7(b) that the velocities in the region of  $0.2 \text{ m} \leq x \leq 0.25 \text{ m}$  are larger than those in the other region due to the existence of the stack, which narrows the flow channel.

Figures 8 and 9 present the temperature fields and the velocity fields near the stack when the air volume is under the limit cycle condition. From fig. 8, it can be found that the temperatures at different phases in the region on the left side of the stack are much smaller than 1000 K, and will increase with the decrease of the distance from the stack. At the same time, the temperature in the region on the right side of the stack is almost 1000 K due to the heating of the stack. Moreover, at a given location, the variation of the temperature with the phase (time) is limited. On the other hand, the velocity fields are very complex and the variation of the velocity field with the phase (time) is significant.

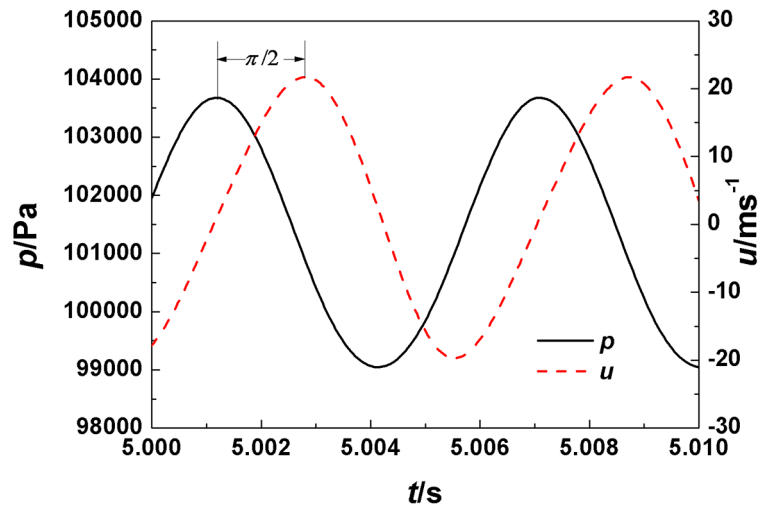


Fig. 5. Pressure and velocity waveforms at point A ( $x = 0.225$  m,  $y = 0.003$  m) under the limit cycle condition.

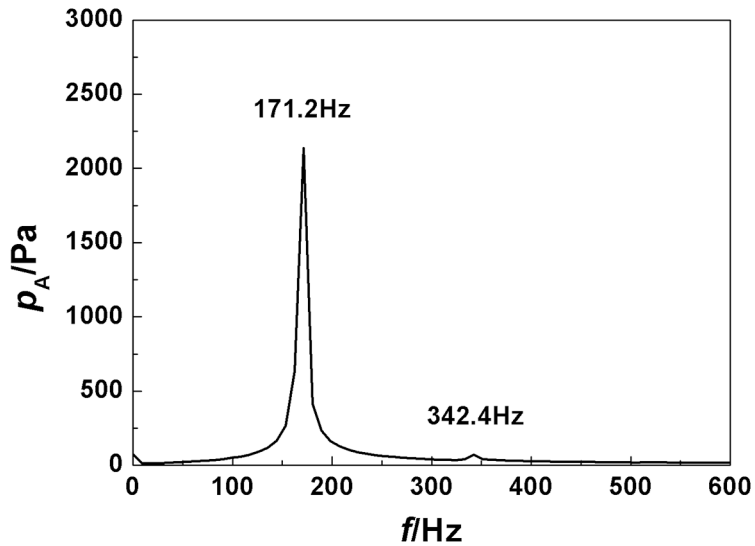


Fig. 6. FFT of the pressure signal at point A ( $x = 0.225$  m,  $y = 0.003$  m) under the limit cycle condition.

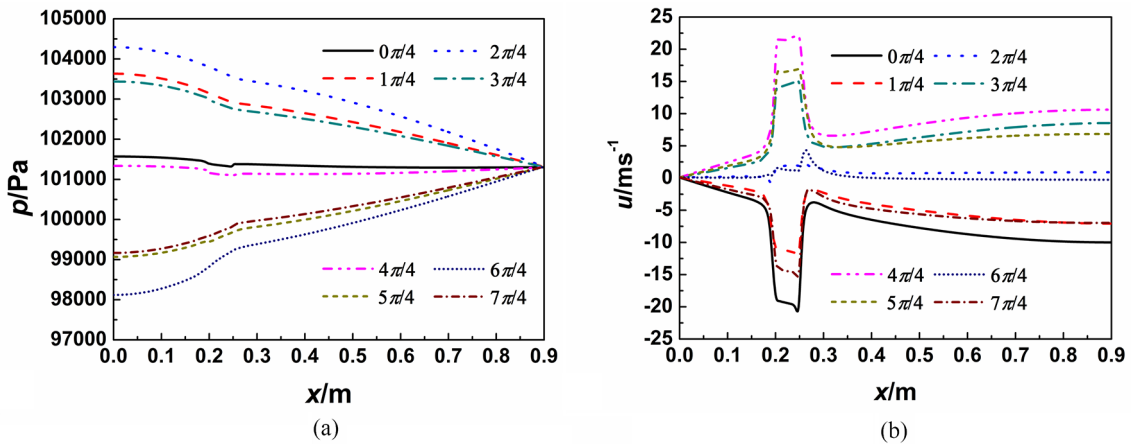
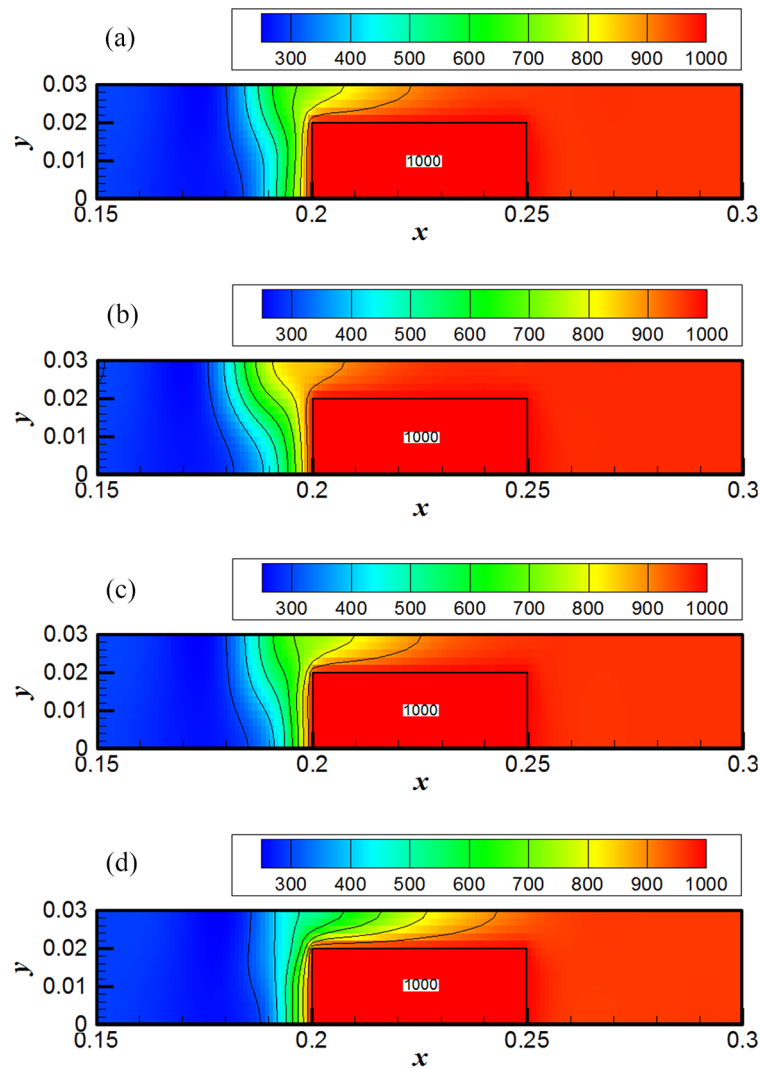


Fig. 7. Instantaneous distributions of the (a) pressure and (b) velocity along the  $x$ -direction of the Rijke tube at  $y = 0.03$  mm under the limit cycle condition.



**Fig. 8.** Instantaneous temperature fields near the stack at four phases under the limit cycle condition. (a) 0; (b)  $\pi/2$ ; (c)  $\pi$ ; (d)  $3\pi/2$ . ( $x/m$ ,  $T/K$ ).

It should be noted that the velocity of the air in the Rijke tube is a combination of the inlet flow velocity (0.1 m/s) with right direction and the oscillating velocity of the air volume (changing direction periodically). In fig. 9(a) at phase 0, the oscillating velocity in the  $x$ -direction (right to left) is much larger than the given inlet velocity in  $+x$ -direction (left to right). As a result, the direction of the main flow near the stack is from right to left and no obvious vortex in the flow field is found. One quarter cycle later, in fig. 9(b) at phase  $\pi/2$ , the oscillating velocity of the air decreases and changes its direction from left to right. Then, the main flow become slowly, and a forward vortex and a backward vortex can be seen near the stack. Another quarter cycle later, in fig. 9(c), the oscillating velocity with the  $+x$ -direction increases, and the combined velocity is significant. In fig. 9(d) at phase  $3\pi/2$ , the oscillating flow inverses to  $-x$ -direction and velocity decreases again. An obvious vortex can be found in the right region of the stack due to the contribution of the oscillating flow and the opposite inlet flow. We denote that the oscillating flow and vortex enhance the heat transfer between the air and the stack in the Rijke tube.

Another interesting phenomenon in the Rijke tube is low Mach number compressible flow. From fig. 9 and the discussion above, one can find that the air in the Rijke tube reach its maximal value at phase  $\pi$  (see fig. 9(c)). The corresponding Mach number contours at the phase  $\pi$  are presented in fig. 10. It can be found that the maximal Mach number is in the upper region of the stack and about 0.035, which is much less than the critical value 0.3 used in the conventional fluid dynamics for the compressible flow. On the other hand, the nonlinear self-excited onset is essentially due to the compressibility of the air volume in the Rijke tube. As a result, the air flows before or under the limit cycle condition in the Rijke tube can be classified as low Mach number compressible fluid flow and heat transfer. And such specific flow will be studied in detail in the future.

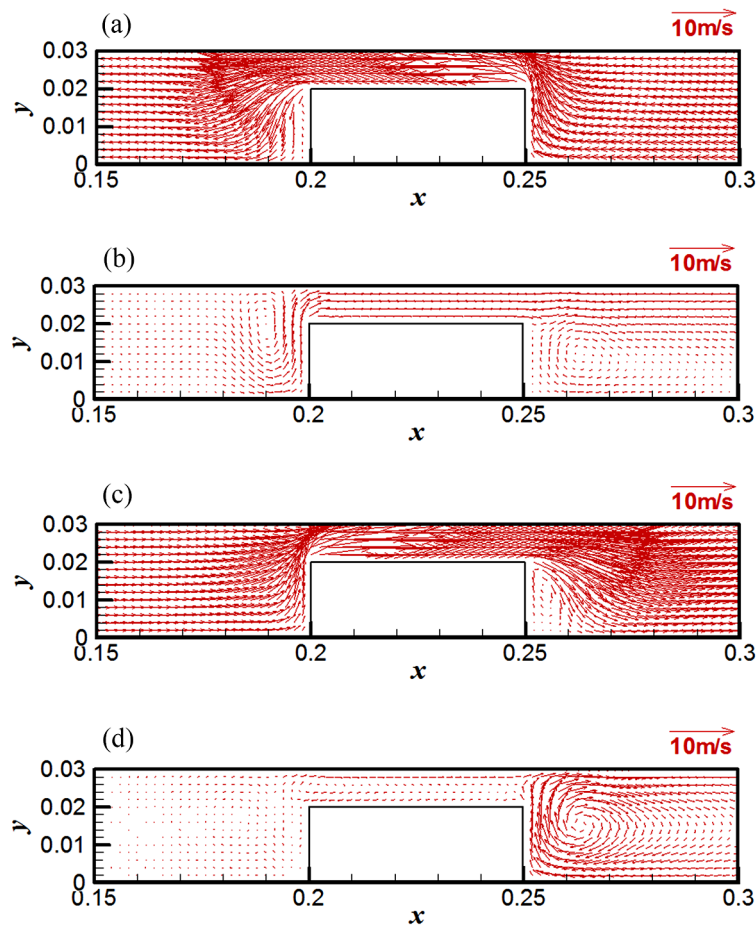


**Fig. 9.** Instantaneous velocity fields near the stack at four phases under the limit cycle condition. (a) 0; (b)  $\pi/2$ ; (c)  $\pi$ ; (d)  $3\pi/2$ . ( $x/m$ ).

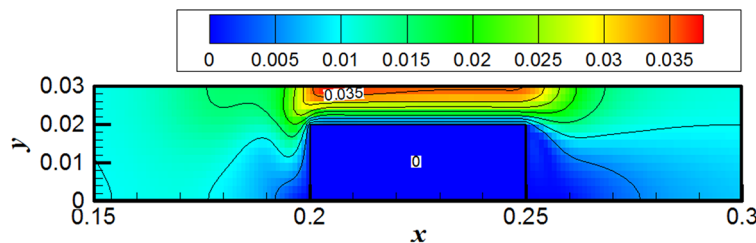


**Fig. 10.** The Mach number contours near the stack at phase  $\pi$  under the limit cycle condition. ( $x/m$ ).

### 5 Conclusion

In this work, a numerical study on the nonlinear thermoacoustic self-excited onset was performed via the LBM. A LBM model for viscous compressible flow and the IMEX FDLBM developed by us were introduced and used to develop a solver. Shared memory programming with OpenMP was also adopted in this solver. An open-open Rijke tube with a constant-temperature stack was simulated with the LBM solver. Details of the boundary treatments are given.

From the numerical results, overall nonlinear onset process is presented significantly in the time histories of the pressure, velocity and temperature at different locations. Self-excited standing wave in the Rijke tube is observed. It is found that the temperature of the air in the main region of the Rijke tube is about 960 K under the limit cycle condition. The length of the Rijke tube along the  $x$ -direction covers a  $1/4$  wavelength of the standing wave and the main component of the standing wave is 171.2 Hz. These numerical results agree well with the theoretical prediction. Instantaneous temperature fields and velocity fields near the stack when the air volume is under its limit cycle condition are presented and discussed. The maximal Mach number in the Rijke tube is about 0.035. The air flows before or under the limit cycle condition in the Rijke tube are regards as the low Mach number compressible flow.

The LBM solver used in this work is being employed for ongoing study on the low Mach number compressible flow and the flow within porous medium in the thermoacoustic engine.

This work was supported by the Key Project of National Natural Science Foundation of China (No. 51436007) and the National Key Basic Research Program of China (973 Program) (2013CB228304).

## References

1. A. Gopinath, N.L. Tait, S.L. Garrett, *J. Acoust. Soc. Am.* **103**, 1388 (1998).
2. C.C. Hantschk, D. Vortmeyer, *J. Sound Vib.* **277**, 511 (1999).
3. C.C. Hantschk, D. Vortmeyer, *Chem. Eng. Technol.* **23**, 758 (2000).
4. B. Entezam, W.K.V. Moorhem, J. Majdalani, *Numer. Heat Transfer A* **41**, 245 (2002).
5. G.Y. Yu *et al.*, *J. Appl. Phys.* **102**, 074901 (2007).
6. L. Kabiraj, R.I. Sujith, *J. Fluid Mech.* **713**, 376 (2012).
7. L. Qiu *et al.*, *Chin. Sci. Bull.* **58**, 1325 (2013).
8. D.M. Sun *et al.*, *Appl. Acoust.* **81**, 50 (2014).
9. K.T. Feldman, *J. Sound Vib.* **7**, 83 (1968).
10. W. Kunz, *Untersuchungen zum anregungsmechanismus thermoakustischer schwingungen am beispiel des Rijke phänomens* (Technische Universität, Berlin, 1981).
11. M.A. Heckl, *Acustica* **72**, 63 (1990).
12. P. Chatterjee *et al.*, *J. Sound Vib.* **283**, 573 (2005).
13. S. Succi, *Lattice Boltzmann equation for fluid dynamics and beyond* (Clarendon Press, Oxford, 2001).
14. G.R. McNamara, G. Zanetti, *Phys. Rev. Lett.* **61**, 2332 (1988).
15. J.M. Buick, C.A. Greated, D.M. Campbell, *Europhys. Lett.* **43**, 235 (1998).
16. D. Haydock, J.M. Yeomans, *J. Phys. A* **34**, 5201 (2001).
17. X.M. Li, R.C.K. Leung, R.M.C. So, *AIAA J.* **44**, 78 (2006).
18. H. Kang, M. Tsutahara, *Int. J. Numer. Methods Fluids* **53**, 629 (2007).
19. D.K. Sun *et al.*, *Chin. Phys. Lett.* **30**, 074702 (2013).
20. Y. Wang, S. Elghobashi, *Respir. Physiol. Neurobiol.* **193**, 1 (2014).
21. Y. Wang *et al.*, *Int. J. Heat Mass Transfer* **51**, 3082 (2008).
22. Y. Wang *et al.*, *Int. J. Numer. Methods Fluids* **59**, 853 (2009).
23. Y. Wang *et al.*, *Int. J. Mod. Phys. C* **21**, 383 (2010).
24. Y. Wang *et al.*, *Int. J. Mod. Phys. C* **18**, 1961 (2007).
25. T. Kataoka, M. Tsutahara, *Phys. Rev. E* **69**, 035701 (2004).
26. Z.L. Guo, C.G. Zheng, B.C. Shi, *Chin. Phys.* **11**, 0366 (2002).
27. L. Pareschi, G. Russo, *J. Sci. Comput.* **25**, 129 (2005).